coatings

MDPI

Article

Epitaxial Stabilization of Perovskite $ATeO_3$ Thin Films

Andreas Herklotz [1,2,*], Florina Stefania Rus [3], Martin M. Koch [1], Kyle M. Grove [2], Michael S. Bowen [2], David P. Cann [2], Kristin Tippey [4] and Kathrin Dörr [1]

1 Institute for Physics, Martin-Luther-University Halle-Wittenberg, 06099 Halle, Germany
2 School of Mechanical, Industrial, and Manufacturing Engineering, Oregon State University, Corvallis, OR 97331, USA; kyle.m.grove@gmail.com (K.M.G.); bowenmic@oregonstate.edu (M.S.B.); cann@oregonstate.edu (D.P.C.)
3 National Institute for Research and Development in Electrochemistry and Condensed Matter, Aurel Paunescu Podeanu Street, No. 144, 300569 Timisoara, Romania; rusflorinastefania@gmail.com
4 Helmholtz-Zentrum Dresden-Rossendorf, Bautzner Landstraße 400, 01328 Dresden, Germany
* Correspondence: herklotza@gmail.com

Abstract: Tellurium oxides of the $ATeO_3$ form typically do not crystallize in perovskite structures. Here, we show that perovskite-like $ATeO_3$ (A = Ca, Sr, Ba) thin films can be grown on perovskite single-crystal substrates via epitaxial stabilization. These films are stable with high optical bandgaps, low dielectric losses, and a high electric breakdown strength. Hysteretic dielectric behavior found in $SrTeO_3$ and $BaTeO_3$ strongly suggests the presence of antiferroelectricity and ferroelectricity, respectively. These properties make perovskite tellurium oxides possibly appealing candidates for thin film coating or insulator materials in advanced microelectronics. Tellurium oxides constitute a largely unexplored class of materials that might show new and interesting functionalities in epitaxial thin-films. Our work encourages new work within this field.

Keywords: perovskite; ferroelectric; chalcogenide

check for updates

Citation: Herklotz, A.; Rus, F.S.; Koch, M.M.; Grove, K.M.; Bowen, M.S.; Cann, D.P.; Tippey, K.; Dörr, K. Epitaxial Stabilization of Perovskite $ATeO_3$ Thin Films. *Coatings* **2023**, *13*, 2055. https://doi.org/10.3390/coatings13122055

Academic Editor: Alicia de Andrés

Received: 21 November 2023
Revised: 2 December 2023
Accepted: 5 December 2023
Published: 7 December 2023

1. Introduction

Ternary oxides have great potential to show properties that make them favorable for diverse applications in the science of materials. As such, perovskites with ABO_3 unit blocks have been largely explored, where A and B are typically metal cations. The stability range of these perovskites can be described surprisingly well using the Goldschmidt factor $t = (r_A + r_B)/\sqrt{2}\,(r_B + r_O)$, where r_A, r_B, and r_O are the ionic radii of the anions and cations, respectively [1]. Goldschmidt originally proposed that materials with $0.8 < t < 1.0$ are typically of a perovskite structure, where a deviation from the ideal value of 1.0 leads to distortions from the ideal cubic perovskite structure. Materials with $t < 0.7$ generally stabilize in other energetically more favorable structures. High-throughput ab-initio calculations and machine learning approaches have recently helped to refine the stability range of perovskites in order to facilitate structural predictions. Figure 1a shows a sketch of the perovskite stability range derived by Filip et al. [2] as a function of the tolerance factor t and the octahedral factor $\mu = r_B/r_O$.

Based on this stability range, ternary oxides with alkaline earth metal ions A = Ca, Sr, Ba, and B-site tellurium cations fall on the edge of this perovskite stability range (see Figure 1a). According to Shannon et al. [3], the ionic radius of Te^{4+} (0.97 pm) is comparable to that of Ce^{4+} (0.94 pm). It is therefore reasonable to assume a similar structural behavior between $ATeO_3$ and $ACeO_3$ compounds. $SrCeO_3$ and $BaCeO_3$ both stabilize in perovskite structures with large oxygen octahedral rotations, whereas perovskite $CaCeO_3$ is unstable and decomposes to CaO and CeO_2 [4]. However, $ATeO_3$ does not form perovskite structures in bulk form. Due to the high covalent character of Te ions, tellurium oxides typically form highly complex phases with multiple polymorphs in close energetic proximity to the ground state phase. A particularly interesting example is $SrTeO_3$, with a room temperature

non-polar phase that transforms into a ferroelectric phase above 310 °C [5]. The dielectric constant of $SrTeO_3$ reaches a value of about 10^4 near the Curie temperature of 485 °C, comparable to the highest dielectric constant in the prototype ferroelectric $BaTiO_3$ [6].

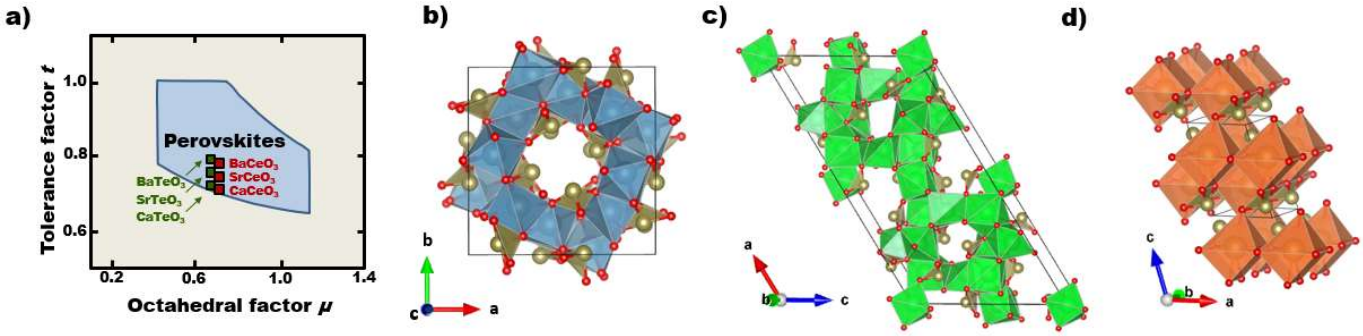

Figure 1. (**a**) Stability range of perovskites, as proposed by Filip et al. [2]. The positions of $ATeO_3$ and $ACeO_3$ according to the ionic radii taken from Shannon et al. [3] are shown. (**b**–**d**) Ground state crystal structures of $CaTeO_3$, $SrTeO_3$, and $BaTeO_3$. All of these bulk structures are characterized by TeO_3 pyramids, as opposed to the TeO_6 octahedra that would be found in perovskite structures.

This example suggests that new phases and functionalities might be found in thin films. However, to the best of our knowledge, epitaxial $AteO_3$ thin films have not been studied so far. In this paper, we report the successful growth of epitaxial ternary tellurium oxide thin films via pulsed laser deposition. We show experimental and theoretical evidence that $ATeO_3$ can be epitaxially stabilized as perovskites in thin films grown on single-crystal substrates.

2. Materials and Methods

2.1. Thin Film Preparation

Stoichiometric targets of $CaTeO_3$, $SrTeO_3$ and $BaTeO_3$ were prepared via standard solid-state synthesis. The targets were found to be of their bulk phases (see Figure 1b–d), with structural and dielectric properties closely resembling those reported in the literature [7–9]. Then, roughly 100 nm thick films were grown via pulsed laser deposition at a temperature of 550 °C and an energy density of 1.5 J/cm^2. The oxygen pressure was p_{O2} = 0.1 mbar for $CaTeO_3$ and $SrTeO_3$, and 10^{-4} mbar for $BaTeO_3$. After growth, the samples were annealed for 5 min and cooled in 600 mbar of oxygen to ensure full oxygenation of the films. The laser deposition was carried out onto single-crystalline $SrTiO_3$ (STO) and $LaAlO_3$ (LAO) substrates with (001) orientation.

2.2. Characterization

X-ray diffraction (XRD) was performed with a *Bruker Advance D8* (Billerica, MA, USA) diffractometer and a copper source. Density functional theory (DFT) calculations were performed with the Quantum Espresso software package version 6.4. [10,11] and are based on Perdew–Burke–Ernzerhof (PBE) exchange functionals and a 6 × 6 × 6 Monkhorst k-point grid. Projector augmented-wave pseudopotentials with an energy cut-off of 700 eV were employed. Raman measurements were only conducted for the films on LAO (001) substrates, since the scattering of $SrTiO_3$ substrates is too large. A *Nanomics Imaging Multiview 1000^{TM}* setup was used with a 532 nm laser.

Optical properties of the films have been determined via variable angle spectroscopic ellipsometry using a *J.A. Woolam M-2000*. The recorded ellipsometry data are fitted to a simple two-layer model consisting of the substrate and a film with a certain film surface roughness. The film layers are first approximated using a Cauchy model in order to obtain a good starting point for refinement using a Kramers–Kronig consistent B-spline fit with 19 data points over the full energy range. The B-spline fit was necessary accurately capture

the absorption above the band gaps [12]. The substrates' optical properties were fixed to dielectric functions, independently determined by fitting the data of the bare substrates.

In order to perform an electrical characterization, $ATeO_3$ films were grown on Nb–$SrTiO_3$ substrates and capped with 50 × 50 μm^2 large Au-top electrodes deposited by magnetron sputtering. Capacitance-voltage hysteresis loops were then recorded with an *HP Agilent 4278A LCR* meter. A low signal voltage and frequency of 0.2 V and 100 kHz, respectively, was used. The dielectric constants were calculated based on the top electrode area and the thin film thickness. Polarization loops were measured with an *aixACCT TF Analyzer 1000*.

3. Results and Discussion

3.1. X-ray Diffraction

Figure 2a,b show wide-angle XRD 2θ-θ scans of the $ATeO_3$ films grown on (001)-oriented STO and LAO substrates, respectively. All films are phase pure and grown epitaxially; i.e., the XRD pattern can fully be explained by a single structure with a homogeneous crystal orientation. At first sight, the XRD patterns resembled those of typical patterns of perovskite thin films grown with cube-on-cube epitaxy. In order to corroborate this observation, the existence of a variety of peak reflections was checked. It was found that for all three materials, all peak reflections were consistent with a perovskite structure.

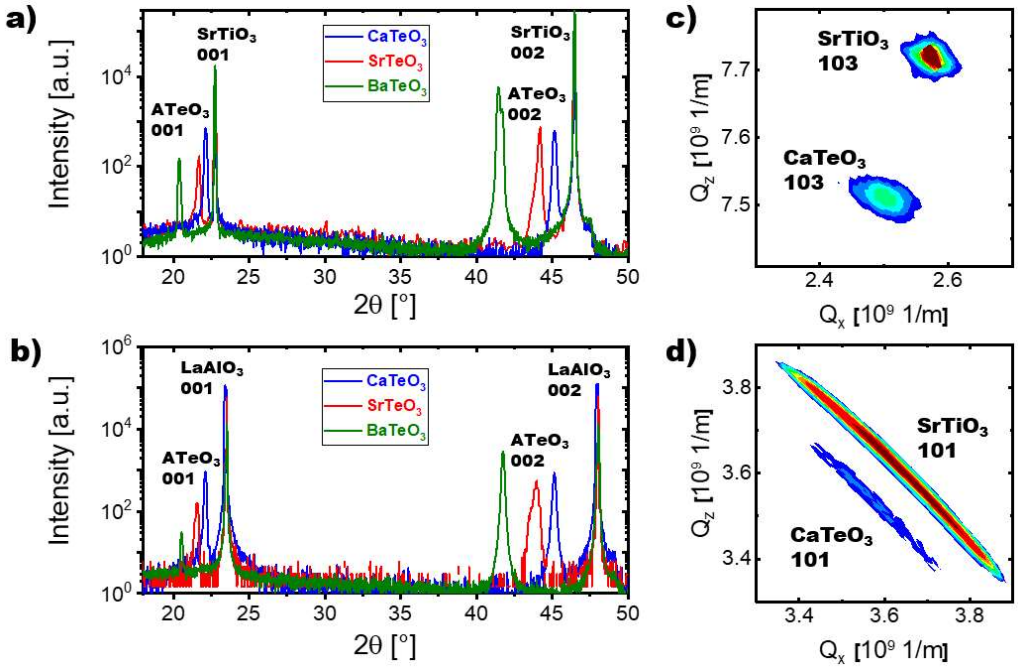

Figure 2. (**a**,**b**) XRD 2θ-θ scans on $ATeO_3$ films grown on STO (001) and LAO (001), respectively. (**c**,**d**) Reciprocal space maps around the pseudocubic (103) and (101) reflections of the $CaTeO_3$/STO (001) film, respectively. The (101) peaks are broadened due to the measurement geometry, not the film or substrate quality.

Pseudocubic lattice parameters of the perovskite films were determined from reciprocal space maps measured around the $(103)_{pc}$ reflections. Exemplary maps for the $CaTeO_3$/STO (001) film are shown in Figure 2c,d, respectively. It is apparent that the films are not coherently strained to the substrate, but show a large degree of strain relaxation. The calculated pseudocubic lattice parameters are listed in Table 1. In general, the lattice parameters increase within the Ca–Sr–Ba series, as can be expected according to the increasing ion size. For $CaTeO_3$, the in-plane and out-of-plane lattice parameters (*a* and *c*) are similar, which indicates full strain relaxation. In contrast, $SrTeO_3$ and $BaTeO_3$ show some degree of tetragonality. Apart from incomplete strain relaxation, this fact could be attributed to a

variety of other reasons. For example, the sustained tetragonality could be due to a thermal expansion mismatch between the substrate and the film material. A second cause could be the creation of oriented defects during the deposition of non-stoichiometric films, as this has been previously observed in $BaTiO_3$ films [13]. Lastly, the films might show polar behavior, and the tetragonality could be a reflection of ferroelectric displacement. Since the out-of-plane lattice parameter is smaller than the in-plane parameter, the ferroelectric polarization would be oriented in the film plane.

Table 1. List of pseudocubic lattice parameters determined from the positions of XRD film peaks.

	$CaTeO_3$ /STO	**$CaTeO_3$ /LAO**	**$SrTeO_3$ /STO**	**$SrTeO_3$ /LAO**	**$BaTeO_3$ /STO**	**$BaTeO_3$ /LAO**
a [Å]	4.010	4.012	4.160	4.151	4.356	4.336
c [Å]	4.014	4.014	4.107	4.117	4.342	4.324

We have observed that the films only grow in perovskite form when grown on perovskite substrates, while no epitaxial growth is observed on other substrates with similar lattice parameters (for example, MgO). We thus deduct that the structural similarity is important. For the $ATeO_3$ films, it is energetically more favorable to stay in a perovskite structure than introduce large amount of defects and heavily reconstruct at the interface. In summary, our XRD results suggest that perovskite $ATeO_3$ films can be stabilized with epitaxial growth on perovskite substrates. Our measurements also show that the phases remain stabled over the months and no noticeable destabilization was observed in a humid atmosphere. We do note, however, that the $BaTeO_3$ films needed to be grown in a low-oxygen pressure environment to produce a decent crystalline quality. We speculate that during PLD growth, this tellurate is in competition with another oxide with a different tellurium valence state, most likely $BaTeO_4$.

3.2. Density Functional Theory Calculations

DFT calculations were performed on the bulk $ATeO_3$ phases and their perovskite counterparts. Since perovskites with a tolerance factor of $t < 1$ typically lower their energies through oxygen octahedral rotations, it is very likely that the $ATeO_3$ films do not stabilize in the ideal perovskite structure. A complete exploration of the full phase space of various octahedral rotation patterns using DFT would be beyond the scope of this work. Therefore, we restrained our calculations to the ideal cubic perovskite phase (space group *Pm3m*) and the perovskite phase with an $a^-a^-c^+$ octahedral rotation pattern (space group *Pnma*). The latter is often found in perovskites with large B-site ions (i.e., low tolerance factors), such as $SrCeO_3$ or $SrZrO_3$.

The calculated energy differences between all three structures are depicted in Figure 3. The DFT results show three results that we highlight as significant:

1. The distorted perovskite phases of all three $ATeO_3$ compounds are very close in energy to their bulk ground states, with energy differences <50 meV/atom. These small energy differences directly suggest that the perovskite structures can be energetically favorable over the bulk phases, which are geometrically less compatible with perovskite single-crystal substrates and would require large lattice alterations at substrate–film interfaces.
2. The energy difference between the ideal *Pm3m* perovskite phases and the bulk phases reduces with increases in the A-site ion radius, from $CaTeO_3$, over $SrTeO_3$, to $BaTeO_3$. This observation is in agreement with the fact that the $ATeO_3$ moves farther into the perovskite stability range as the tolerance factor is increased.
3. The energy difference between the cubic *Pm3m* and the orthorhombic *Pnma* phases decreases with increases in the A-site ion radius. This is another indication that the energy gained through oxygen octahedral rotations and tilts is reduced as the tolerance factor approaches one. This same trend can, for example, be observed in the

$AZrO_3$ series, where $CaZrO_3$ has strong $a^-a^-c^+$ octahedral rotation, while $BaZrO_3$ has an ideal cubic perovskite structure.

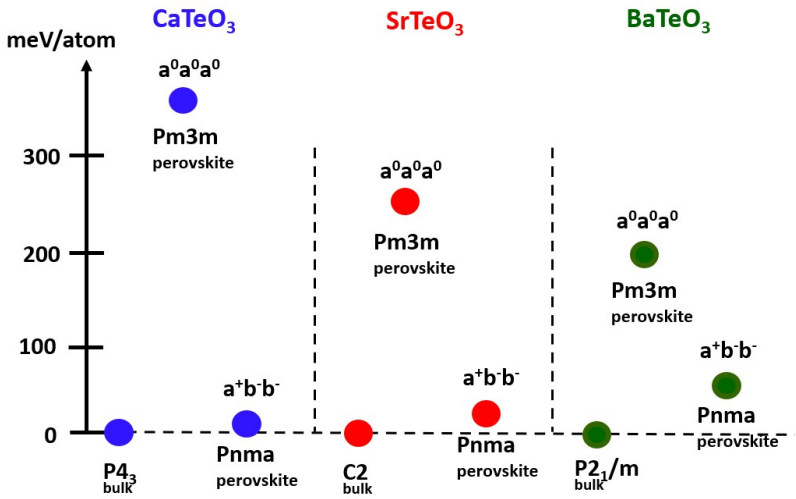

Figure 3. Total energy difference between the perovskite phases (*Pm3m* and *Pnma*) and the bulk $ATeO_3$ phases. The energy differences for the *Pnma* phases are <50 meV/atom, which is generally seen as barrier that can be overcome with epitaxial stabilization.

It should be noted that further theoretical and experimental work is needed to determine the exact lattice structure of the perovskite $ATeO_3$ phases. Since Te^{4+} is stereoactive, cation displacements may be present that would lead to polar or anti-polar phases.

3.3. Raman Studies

Raman spectra of both the actual samples and the bare substrates were recorded in order to subtract the substrates' background and obtain spectra of the film material. These results are presented in Figure 4. For all three films, we find a strong Raman peak near 720–750 cm^{-1}. A weaker peak with varying prominence and width is observed about 100 cm^{-1} below the main peak. Especially for $SrTeO_3$, a broader shoulder is evident that is reminiscent of second-order scattering in $SrTiO_3$ [14].

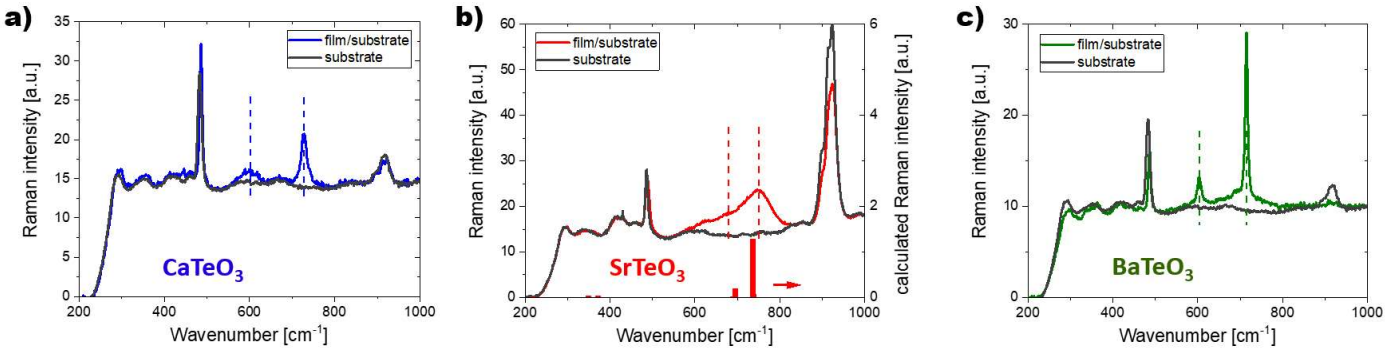

Figure 4. (**a**–**c**) Raman spectra of $CaTeO_3$, $SrTeO_3$, and $BaTeO_3$ films grown on LAO (001) substrates, respectively. Raman intensities calculated via DFT are shown for $SrTeO_3$.

Raman modes in the 500–800 cm^{-1} wavenumber range can usually be attributed to Te–O stretching motions [15]. The typical Te–O_x geometries in tellurium oxides are TeO_3 pyramids, TeO_4 disphenoids, and TeO_6 octahedra. The symmetric stretching Ag mode of the TeO_3 pyramid, as is present in, for example, bulk $BaTeO_3$, has previously been assigned to a Raman peak at 750 cm^{-1}, i.e., one significantly higher than in our film [16]. Also, an anti-stretching mode of similar intensity is observed at lower wavenumbers, which is

not present in our spectra. We therefore conclude that the presence of TeO_3 pyramids is unlikely in the $AteO_3$ films.

TeO_4 disphenoids are present in both the α- and γ-phase of TeO_2. For both of these two phases, the most intense Raman line is located below 680 cm^{-1} and multiple strong lines are found in the range of 400–600 cm^{-1} [17]. This observation is in disagreement with our Raman data and we deduce that TeO_4 disphenoids are unlikely to be present in all $ATeO_3$ films.

The Raman spectra of tellurium oxides with TeO_6 octahedra, such as Ln_2TeO_6 (Ln = Y, La, Sm) (Ref. [18]), do show a strong Raman peak at 720–750 cm^{-1} and a second weaker peak about 100 cm^{-1} lower. Thus, our data suggest the presence of TeO_6 octahedra in our $ATeO_3$ films.

We have also used DFT to calculate Raman wavenumbers and intensities for *Pnma*-$SrTeO_3$ (see Figure 4b). The strong A_g Raman mode at 750 cm^{-1} agrees very well with the experimentally observed peak. The calculation also provides a pair of modes at 710 cm^{-1}, which could be assigned to the weaker peak found in the measurement. Computationally, much more demanding calculations would be necessary to increase the reliability of these Raman calculations and include second-order effects. However, we take the DFT results presented here as another indication that the tellurium in the $ATeO_3$ films is coordinated with O_6 octahedra, as one would expect in a perovskite.

3.4. Optical Properties

Optical properties of the films have been determined using variable angle spectroscopic ellipsometry. Figure 5 shows a Tauc plot of the absorption coefficient α for the $ATeO_3$ films grown on STO (001) substrates. All three perovskite films show little absorption at lower energies and a sharp increase above their band gaps. This behavior is typical for perovskite large-bandgap insulators. A linear extrapolation of the absorption coefficient to zero provides a rough estimate of the optical band gap. The perovskite $BaTeO_3$ and $SrTeO_3$ films have a gap of around 3.9 and 4.2 eV, respectively, while that of $CaTeO_3$ is even higher. This indicates that these films could be used as transparent, and possibly highly insulating, buffer layers in perovskite heterostructures. The increase in the band gap with decreasing ion size is consistent with general trends in metal oxides, such as, for example, the $ATiO_3$ and $ACeO_3$ families [19,20].

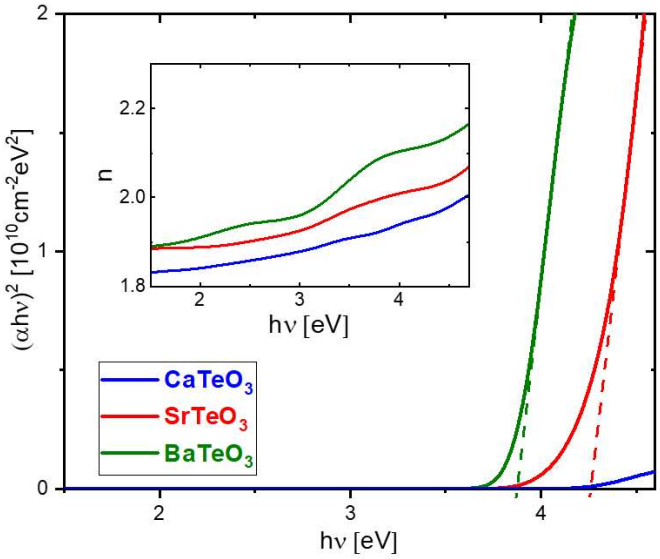

Figure 5. Tauc plot of the absorption coefficient α. Dashed lines represent linear approximations to the experimental data in order to obtain estimates of the optical band gaps. The inset graph shows the refractive index as a function of the photon energy.

The refractive index of the $ATeO_3$ films, as determined from the ellipsometry, is plotted in inset of Figure 5. A trend of an increasing refraction index with increasing photon energy and ion size is observed.

3.5. Dielectric Characterization

The relative dielectric permittivity ε_r as a function of bias voltage is shown in Figure 6a for all three materials. We find that $CaTeO_3$ shows predominately dielectric or paraelectric behavior with a weak non-linearity. $SrTeO_3$, on the other hand, exhibits a clear hysteretic behavior, with a loop shape that is typical for antiferroelectrics. In order to corroborate this finding, a polarization loop was measured. The loop is depicted in Figure 6b. When the data are corrected for parasitic capacitance and leakage current, clear characteristics of an antiferroelectric hysteresis loop become evident.

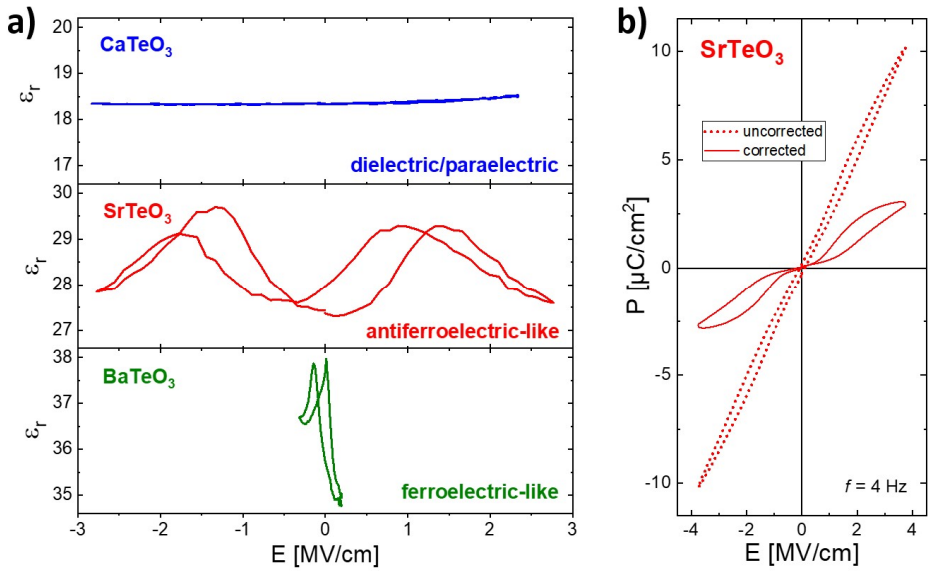

Figure 6. (**a**) Relative dielectric permittivities as a function of the applied electric field. Antiferroelectric- and ferroelectric-like behavior is seen for $SrTeO_3$ and $BaTeO_3$, respectively. (**b**) Polarization loop of $SrTeO_3$, as measured and after correction for parasitic capacitance and leakage currents. This polarization loop is reminiscent of antiferroelectric behavior.

A notable hysteretic behavior is also seen in the dielectric constant of $BaTeO_3$. In this case, the butterfly-like hysteresis loop is reminiscent of ferroelectric behavior. Unfortunately, we were not able to obtain clean polarization loops to confirm this observation. We also note that piezoresponse force microscopy was conducted for all three films, but it revealed no clear evidence of ferroelectric behavior.

All three materials exhibit quite a high dielectric permittivity (ε_r = 18–37). Due to its large bandgap, $CaTeO_3$ in particular shows low dielectric losses and a high electric breakthrough strength of several MV/cm. This observation makes it a possible candidate to consider as a gate oxide or coating material for thin-film devices. The increasing ε_r with increasing ion size is a further indication of polar tendencies in the $ATeO_3$ perovskites and is typical for metal oxides. Good examples of this are titanates, where $CaTiO_3$ and $SrTiO_3$ are incipient ferroelectrics and a ferroelectric state can be induced by small lattice distortions. $BaTiO_3$ is a classic ferroelectric.

Ferroelectric and antiferroelectric behavior are of interest for potential applications and deserve further investigation. Further optimization of thin film growth conditions and capacitor geometry is needed to gain a conclusive result. Nevertheless, our initial data indicate that the stereoactive Te^{4+} ions in perovskite $ATeO_3$ films promotes polar behavior.

4. Conclusions

Epitaxial films of $ATeO_3$ (A = Ca, Sr, Ba) were grown on perovskite single-crystal substrates. X-ray diffraction and Raman spectroscopy were used to show that the epitaxial films are stabilized in perovskite structures, phases that are not observed in bulk ceramics for these materials. An array of DFT calculations show small total energy differences (<50 meV/atom) between the perovskite phases and their bulk structures. Our measurements show that the films have large optical bandgaps, high dielectric permittivities, and low dielectric losses. They can be considered as potential materials to use as insulators in thin film applications. Hysteretic behavior was found in the $SrTeO_3$ and $BaTeO_3$ films, strongly suggesting the presence of antiferroelectricity and ferroelectricity, respectively. The formation of ternary tellurium oxides with perovskite structures can motivate future exploration of new functionalities based on the properties of their stereoactive chalcogen cations.

Author Contributions: Conceptualization, A.H.; Methodology, K.M.G.; Formal analysis, M.S.B.; Investigation, A.H. and F.S.R.; Writing—original draft, A.H.; Writing—review & editing, M.M.K., D.P.C. and K.T.; Supervision, A.H.; Project administration, D.P.C. and K.D.; Funding acquisition, A.H. All authors have read and agreed to the published version of the manuscript.

Funding: A. Herklotz was funded by the German Research Foundation (DFG)—grant no. HE8737/1-1. The work of F.S. Rus was supported by a mobility grant from the Romanian Ministry of Research and Innovation, CNCS-P1-1.1-MC-2019-1374, within PNCDI III.

Data Availability Statement: The data that support the findings of this study are available from the corresponding author upon reasonable request.

Conflicts of Interest: The authors declare no conflict of interest.

References

1. Goldschmidt, V.M. Die Gesetze der Krystallochemie. *Naturwissenschaften* **1926**, *14*, 477–485. [CrossRef]
2. Filip, M.R.; Giustino, F. The geometric blueprint of perovskites. *Proc. Natl. Acad. Sci. USA* **2018**, *115*, 5397–5402. [CrossRef] [PubMed]
3. Shannon, R.D. Revised effective ionic radii and systematic studies of interatomic distances in halides and chalcogenides. *Acta Cryst. A* **1976**, *32*, 751–767. [CrossRef]
4. Oka, R.; Tsukimori, T.; Inoue, H.; Masui, T. Perovskite-type $ALnO_3$ (A = Ca, Sr, Ba; Ln = Ce, Pr, Tb) oxides as environmentally friendly yellow pigments. *J. Ceram. Soc. Jpn.* **2017**, *125*, 652–656. [CrossRef]
5. Yamada, T.; Iwasaki, H. New ferroelectric compound $SrTeO_3$. *Appl. Phys. Lett.* **1972**, *21*, 89–90. [CrossRef]
6. Vijatović Petrović, M.M.; Bobić, J.D.; Stojanović, B. History and Challenges of Barium Titanate: Part II. *Sci. Sinter.* **2008**, *40*, 235–244. [CrossRef]
7. Stöger, B.; Weil, M.; Zobetz, E.; Giester, G. Polymorphism of $CaTeO_3$ and solid solutions $Ca_xSr_{1-x}TeO_3$. *Acta Crystallogr. B* **2009**, *65*, 167–181. [CrossRef] [PubMed]
8. Zavodnik, V.E.; Ivanov, S.A.; Stash, A.I. The α-phase of $SrTeO_3$ at 295 K. *Acta Cryst. E* **2007**, *63*, i75–i76. [CrossRef]
9. Koçak, M.; Platte, C.; Trömel, M. Über Verschiedene Formen von $BaTeO_3$. *Z. Anorg. Allg. Chem.* **1979**, *453*, 93–97. [CrossRef]
10. Giannozzi, P.; Baroni, S.; Bonini, N.; Calandra, M.; Car, R.; Cavazzoni, C.; Ceresoli, D.; Chiarotti, G.L.; Cococcioni, M.; Dabo, I.; et al. QUANTUM ESPRESSO: A modular and open-source software project for quantum simulations of materials. *J. Phys. Condens. Matter* **2009**, *21*, 395502. [CrossRef] [PubMed]
11. Giannozzi, P.; Andreussi, O.; Brumme, T.; Bunau, O.; Buongiorno Nardelli, M.; Calandra, M.; Car, R.; Cavazzoni, C.; Ceresoli, D.; Cococcioni, M.; et al. Advanced capabilities for materials modelling with Quantum ESPRESSO. *J. Phys. Condens. Matter* **2017**, *29*, 465901. [CrossRef] [PubMed]
12. Manzoor, S.; Häusele, J.; Bush, K.A.; Palmstrom, A.F.; Carpenter, J.; Yu, Z.J.; Bent, S.F.; Mcgehee, M.D.; Holman, Z.C. Optical modeling of wide-bandgap perovskite and perovskite/silicon tandem solar cells using complex refractive indices for arbitrary-bandgap perovskite absorbers. *Opt. Express* **2018**, *26*, 27441–27460. [CrossRef] [PubMed]
13. Damodaran, A.R.; Breckenfeld, E.; Chen, Z.; Lee, S.; Martin, L.W. Enhancement of Ferroelectric Curie Temperature in $BaTiO_3$ Films via Strain-Induced Defect Dipole Alignment. *Adv. Mater.* **2014**, *26*, 6341–6347. [CrossRef] [PubMed]
14. Perry, C.H.; Fertel, J.H.; McNelly, T.F. Temperature Dependence of the Raman Spectrum of $SrTiO_3$ and $KTaO_3$. *J. Chem. Phys.* **2004**, *47*, 1619. [CrossRef]
15. Smirnov, M.; Kuznetsov, V.; Roginskii, E.; Cornette, J.; Dutreilh-Colas, M.; Noguera, O.; Masson, O.; Thomas, P. Raman spectra and structural peculiarities of TeO_2-TeO_3 mixed oxides. *J. Phys. Condens. Matter* **2018**, *30*, 475403. [CrossRef] [PubMed]
16. Li, Y.; Han, Y.; Ma, Y.; Zhu, P.; Wang, X.; Gao, C. Pressure effects on grain boundary, electrical and vibrational properties of the polycrystalline $BaTeO_3$. *EPL* **2012**, *98*, 66006. [CrossRef]

17. Bataliotti, M.D.; Costa, F.B.; Minussi, F.B.; Araújo, E.B.; de Lima, N.B.; Moraes, J.C.S. Characterization of tellurium dioxide thin films obtained through the Pechini method. *J. Sol-Gel Sci. Technol.* **2022**, *103*, 378–385. [CrossRef]
18. Llanos, J.; Castillo, R.; Barrionuevo, D.; Espinoza, D.; Conejeros, S. The family of Ln_2TeO_6 compounds (Ln=Y, La, Sm and Gd): Characterization and synthesis by the Pechini sol–gel process. *J. Alloys Compd.* **2009**, *485*, 565–568. [CrossRef]
19. Dejneka, A.; Tyunina, M.; Narkilahti, J.; Levoska, J.; Chvostová, D.; Jastrabík, L.; Trepakov, V. Tensile strain induced changes in the optical spectra of $SrTiO_3$ epitaxial thin films. *Phys. Solid State* **2010**, *52*, 2082–2089. [CrossRef]
20. Goubin, F.; Rocquefelte, X.; Whangbo, M.-H.; Montardi, Y.; Brec, R.; Jobic, S. Experimental and Theoretical Characterization of the Optical Properties of CeO_2, $SrCeO_3$, and Sr_2CeO_4 Containing Ce^{4+} (f0) Ions. *Chem. Mater.* **2004**, *16*, 662–669. [CrossRef]